





Article

In Situ Mo(Si,Al)₂-Based Composite through Selective Laser Melting of a MoSi₂-30 wt.% AlSi10Mg Mixture

Tatevik Minasyan ^{1,2,*} , Sofiya Aydiyanyan ¹ , Ehsan Toyserkani ²  and Irina Hussainova ^{1,*} 

¹ Department of Mechanical and Industrial Engineering, Tallinn University of Technology, Ehitajate 5, 19086 Tallinn, Estonia; sofiya.aydiyanyan@taltech.ee

² Multi-Scale Additive Manufacturing Laboratory, Department of Mechanical and Mechatronics Engineering, University of Waterloo, 200 University Ave., West Waterloo, ON N2L 3G1, Canada; ehsan.toyserkani@uwaterloo.ca

* Correspondence: tatevik.minasyan@taltech.ee (T.M.); irina.hussainova@taltech.ee (I.H.)

Received: 2 August 2020; Accepted: 19 August 2020; Published: 23 August 2020



Abstract: The laser power bed fusion approach has been successfully employed to manufacture Mo(Si,Al)₂-based composites through the selective laser melting of a MoSi₂-30 wt.% AlSi10Mg mixture for high-temperature structural applications. Composites were manufactured by leveraging the in situ reaction of the components during printing at 150–300 W laser power, 500–1000 mm·s⁻¹ laser scanning speed, and 100–134 J·mm⁻³ volumetric energy density. Microcomputed tomography scans indicated a negligible induced porosity throughout the specimens. The fully dense Mo(Si_{1-x},Al_x)₂-based composites, with hardness exceeding 545 HV1 and low roughness for both the top (horizontal) and side (vertical) surfaces, demonstrated that laser-based additive manufacturing can be exploited to create unique structures containing hexagonal Mo(Si_{0.67}Al_{0.33})₂.

Keywords: selective laser melting; molybdenum disilicide; composite; aluminum alloy; computed tomography; surface roughness

1. Introduction

Molybdenum disilicide MoSi₂ is regarded as a promising material for a wide variety of industrial applications due to its combination of outstanding properties, such as its high melting point (2293 K), moderate density (6.24 g·cm⁻³), excellent intermediate- and high-temperature oxidation resistance, and metallic-like high electrical and thermal conductivity [1]. Exploitation of these properties opens up the prospect for the development of composites with tailored mechanical and physical behaviours. Aluminum is one of the most favorable alloying additions for MoSi₂, which may enhance the high-temperature oxidation resistance, fracture toughness, creep resistance, and low-temperature ductility of MoSi₂, along with introducing a more metallic character to the compound [2].

The main processing routes explored so far for preparation of Mo(Si,Al)₂ are arc melting [3–6], self-propagating high-temperature synthesis (SHS) [7–10], hot pressing [11], spark plasma sintering (SPS) [12], and some others [13], as specified in Table 1.

Table 1. Methods of Mo(Si,Al)₂ fabrication.

Initial Reagents	Preparation Technique	Final Product	Important Notes	Refs.
Mo + 2(1 - x)Si + 2xAl x = 0.14; 0.15; 0.28; 0.37	Arc melting of plates of the constituent elements Mo, Si, and Al in argon.	Mo(Si _{1-x} Al _x) ₂ (0.11 < x < 0.55) x = 0.14; 0.15; 0.28; 0.37	The substitution of Si with Al gives Mo(Si _{1-x} Al _x) ₂ of the C40 structure with a large homogeneity in the range of 0.11 < x < 0.55	[3]
33.3 at.% Mo + 44.2 at.% Si + 22.5 at.% Al	Arc melting	C40 Mo(Al _{0.5} Si _{0.5}) ₂ and C54 MoAl _{1.3} Si _{0.7} phases	Addition of Al as a substitution for Si leads to formation of the higher symmetry C40 and C54 phases	[4]
Mo + 2(1 - x)Si + 2xAl x = 0.0075–0.225	Arc melting	Mo(Si _{0.9925} Al _{0.0075}) ₂ Mo(Si _{0.985} Al _{0.015}) ₂ Mo(Si _{0.925} Al _{0.075}) ₂ Mo(Si _{0.85} Al _{0.15}) ₂ Mo(Si _{0.775} Al _{0.225}) ₂	Al is soluble in MoSi ₂ up to about x = 0.045. The excess of Al resulted in formation of the C40- or C49-type phases	[5]
Mo + 2Si + (1–2.5 at.%)Al	Arc melting	Mo(Al, Si) ₂ Al(1–2.5 at.%)	The addition of 2 at.% Al increased the high-temperature strength of Mo(Al, Si) ₂ , lowered the brittle to ductile transition temperature, and decreased the hardness	[6]
Mo + 2(1 - x)Si + 2xAl x = 0.01–0.5	Self-propagating high-temperature synthesis (SHS) + hot pressing	Mo(Al _{0.5} Si _{0.5}) ₂ Mo(Al _{0.2} Si _{0.8}) ₂ Mo(Al _{0.05} Si _{0.95}) ₂ Mo(Al _{0.01} Si _{0.99}) ₂	The substitution of 10 wt.% Al for Si yielded equal amounts of Mo(Al, Si) ₂ and MoSi ₂	[7]
Mo-2Si-0.04PTFE-0.88Al Mo-2Si-0.08PTFE-0.88Al	SHS	MoSi ₂ , Al, Mo ₅ Si ₃ , AlF ₃ in MoSi ₂ -Al cermet foam	Porous product	[8]
Mo + 2(1 - x) + 2x x = 0–0.5	SHS + induction plasma spheroidization (IPS)	Mo(Si _{1-x} Al _x) ₂ (x = 0–0.5) x = 0 → nearly pure C11b MoSi ₂ x = 0.1 → C11b C40 0.2 ≤ x ≤ 0.4 → C40 + C11b (trace) x = 0.1 → C40 + C54	Mo(Si, Al) ₂ with C40 structure designed as Mo(Si _{0.6} Al _{0.4}) ₂ with the maximum Al content in SHS. After IPS, the apparent density was remarkable improved	[9]
Mo + 2(1 - x)Si + 2xAl x = 0.0–0.5 mole (0 to 17.86 wt.% Al)	SHS	Mo(Si _{1-x} Al _x) ₂ x = 0.08 → C11b MoSi ₂ + C40 x = 0.2 → nearly pure C40 x = 0.5 → C40 + C54	Up to 2.84 wt.% Al, only C11b's tetragonal phase is present; up to 5.33 wt.% Al, a duplex of C11b/C40 phases is present. Increasing the Al reduces the amount of C11b in the biphasic region. A single C40 hexagonal forms at 7.11 wt.% Al. At 17.86 wt.% Al, orthorhombic C54 (Al ₄ Mo ₃ Si ₂) appears	[10]
Mo + 2(1 - x) + 2x x = 0–0.6	Pseudo-HIP	Mo(Si _{1-x} Al _x) ₂ x = 0 → C11b x = 0.1 → C11b + C40 x = 0.2–0.4 → C40 x = 0.5 → C40 + C54 x = 0.6 → C54	C40 is in the range of x = 0.1–0.5, while C11b is detected at x = 0.1 and C54 at x = 0.5. C11b is identified only at x = 0, while only C54 is detected at x = 0.6	[11]
SHS-ed powders Mo _{1-x} Nb _x Si ₂ (x = 0–0.3), Mo(Si _{1-y} Al _y) ₂ (y = 0–0.3)	SFS at 1350 °C and 40 MPa for 6 min in vacuum	(Mo _{1-x} Nb _x)Si ₂ Mo(Si _{1-y} Al _y) ₂	Addition of Nb at x = 0–0.12 increased the strength and toughness	[12]
Mo plate and molten Al saturated with Si and Mo	Dipping Mo into Al-Si bath at 973 K for 350 ks	Mo plate covered with the layer of Mo(Si, Al) ₂ of Mo:Si:Al = 30:12:58	The needle-like grains grow perpendicular to Mo's surface. The reaction goes through the solution–precipitation process in the Al(Si) liquid between Mo and Mo(Si, Al) ₂ layers	[13]

Different Si/Al ratios in Mo(Si_{1-x}Al_x)₂ yield the formation and development of C40 hexagonal and C54 orthorhombic structures. The duplex C40/C54 phases appear when x = 0.5, while monophasic C54, often designated as Mo₁₀Si₇Al₁₃, is established at x = 0.6, as described in [11]. In [9], a similar trend of C54 phase formation was reported. It was also found that at 17.86 wt.% Al addition, the C54 phase with an Al₄Mo₃Si₂ composition is developed [10]. A higher percentage of Al does not promote the development of monophasic C54, since the segregation of Mo suppresses the combustion synthesis. The formation of C40 Mo(Al_{0.5}Si_{0.5})₂ and the orthorhombic C54 MoAl_{1.3}Si_{0.7}, as a result of the arc-melted mixture of 33.3 at.% Mo, 44.2 at.% Si, and 22.5 at.% Al, is reported in [4]. The Al-rich side of the Mo(Si, Al)₂ composition ends at the Al₈Mo₃ phase, as described in [14].

The main difficulties associated with the processing of MoSi₂-AlSi10Mg composites are the restrictive stoichiometry limits, high melting point, and low-temperature brittleness. Application of additive manufacturing (AM) techniques for the MoSi₂-Al system has not been explored yet. AM through selective laser melting (SLM) provides a wide range of new opportunities for the processing and fabrication of various products with complex constitutional designs and shapes, which are impossible to achieve via any conventional method.

In this paper, an attempt is made to produce Mo(Si,Al)₂-based composites in situ, exploiting the laser power bed fusion of MoSi₂ and AlSi10Mg alloy powders and taking into consideration the successful SLM of MoSi₂ [15,16] and AlSi10Mg [17]. In this context, we demonstrate for the first time the reactive selective laser melting of MoSi₂-30 wt.% AlSi10Mg, which results in fully dense bulks of good quality. This paper discusses the material structure and hardness; however, the high-temperature mechanical properties and oxidation are out of this paper's scope.

2. Experiments

2.1. Powder Preparation and Characterization

For SLM feedstock preparation, combustion-synthesized MoSi₂ powder (99% purity) was mixed with 30 wt.% gas-atomized AlSi10Mg (SLM, Solutions, purity >99%, 15–63 μm) for 3 h using mechanical rotation (20 rpm). The particle size and sphericity analyses of the MoSi₂, AlSi10Mg, and MoSi₂-30 wt.% AlSi10Mg powders were carried out in a CAMSIZER X2 device (MICROTRAC MRB, Haan, Germany), adopting dynamic image analysis (ISO 13322-2 [18]) as the measuring principle using 10 mL of powder. Sphericity is determined as the square of the circularity of a powder particle using the $4\sqrt{A}\cdot P^{-2}$ equation, where P is the measured perimeter of the particle and A is the computed area from the particle projection. The FT4 Powder Rheometer (Freeman Technology, Tewkesbury, UK) was used to determine the basic flowability energy (BFE) of powders and mixture. To define the resistance of a powder to flow, 8 test cycles were run. During each test, the precision blade rotated downwards (at a speed of $-100\text{ mm}\cdot\text{s}^{-1}$) and upwards through the fixed volume of powder to create a flow pattern. The BFE is calculated with the following equation: $\text{BFE} = E_{\text{test}8}$, where $E_{\text{test}8}$ is the energy recorded during downward rotation of the blade for the 8th test. The stability index (SI) is calculated as follows: $\text{SI} = E_{\text{test}8}/E_{\text{test}1}$. The packing density of the mixture was measured by GranuPack (GranuTools, Awans, Belgium). The actual value for the average bulk density at the end of the trials ($\rho[n]$) was measured and the bulk density value for $\rho[\infty]$ was extrapolated.

Differential scanning calorimetry (DSC) analysis was performed to analyze the thermal behavior of MoSi₂-30 wt.% AlSi10Mg powder (70 mg) using a NETZSCH-STA 449 F1 Jupiter (NETZSCH-Gerätebau GmbH, Selb, Germany) thermal analyzer from 25 °C to 1450 °C, with a heating rate of 20 °C·min⁻¹ in an argon atmosphere.

2.2. Selective Laser Melting

Consolidation of the MoSi₂-30 wt.% AlSi10Mg mixture by selective laser melting (SLM) was carried out using a Renishaw AM400 apparatus (Wotton-under-Edge, Gloucestershire, UK), which employs a high-power, continuous-wave, and a laser, modulated to work as a pulse laser. The device is equipped with an Ytterbium laser with a maximum power of 400 W and a wavelength of 1.07 μm. Cylindrical samples with dimensions of 7 mm × 7 mm were built. The meander scan strategy was used, whereby scan patterns rotate by 67° after each printed layer. The whole manufacturing process was carried out inside a chamber containing a precisely controlled atmosphere of argon at an oxygen level below 500 ppm. The hatching distance (h) and laser spot size were set as 85 μm and 90 μm, respectively. The laser power (P) was in the range of 150–300 W and the scanning speed (v) was in the range of 500–1000 mm·s⁻¹ range. The layer thickness (d) was chosen as 35 μm. The process parameters for preparation of the three samples are listed in Table 2.

Table 2. Process parameters for samples S1–S3.

Sample ID	Laser Power (W)	Scanning Speed (mm·s ⁻¹)	Laser Volumetric Energy Density (J·mm ⁻³)	Build Rate (mm ³ ·s ⁻¹)
S1	150	500	100.8	1.48
S2	200	500	134.4	1.48
S3	300	1000	100.8	2.97

The laser volumetric energy density (LED) and build rate were calculated according to $E = P/vhd$ and $BR = vhd$, respectively.

2.3. Bulk Characterization

The density of printed parts was measured by Archimedes' principle (Mettler Toledo ME204, Greifensee, Switzerland) and by calculating the dimensions (digital Vernier caliper of 0.01 mm accuracy, Digital Caliper, KS Tools Werkzeuge-Maschinen GmbH, Heusenstamm, Germany) and weight (Eltra 84 analytical balance, 0.1 mg accuracy, Haan, Germany) of the samples. The size, morphology, and alignment of the pores in the SLM-fabricated samples were inspected via X-ray computed tomography (CT) (ZEISS Xradia 520 Versa 3D X-ray microscope Oberkochen, Germany). The surface roughness analysis was performed using a Keyence VK-X250 profile analyzing confocal laser microscope (Keyence Corporation, Osaka, Japan). On each studied surface, 4 areas with dimensions of 500 $\mu\text{m} \times 700 \mu\text{m}$ were scanned using a 20 \times lens. The maximum height (S_z) and arithmetical mean height (S_a) were averaged for 4 measurements.

Samples were ground and polished by conventional metallographic methods to a 0.5 μm diamond polish and to a finer 0.1 μm finish using a nylon disc and polishing suspension. The morphology and microstructure of the powders and printed bulks were examined by TESCAN VEGA3 (Brno, Czech Republic) and HR-SEM Zeiss Merlin scanning electron microscope (SEM, ZEISS, Oberkochen, Germany) equipped with an EDS detector (Bruker EDX-XFlash6/30, Billerica, MA, USA). Phase compositions were analyzed with the help of an X-ray diffractometer (Siemens/Bruker D5000 X-ray Powder Diffraction (XRD) System, Billerica, MA, USA) with $\text{CuK}\alpha$ radiation in the 2θ range of 20° to 80°. The concentrations of compounds and elements were estimated via the Rietveld refinement method. The Vickers hardness values were measured on the polished surfaces of the printed specimens using a tester (Indentec 5030 SKV, Stourbridge, West Midlands, UK) at a load of 9.8 N, applied over 10 s for 10 indents.

3. Results and Discussion

3.1. Powders

Powder flowability is one of the most influencing parameters affecting the powder bed density, and therefore affecting the produced item quality, including the density and roughness. [15,17]. The powder particle shape, size, and distribution are of primary importance for sintering kinetics and powder bed formation [17,19]. The SEM image of the gas-atomized AlSi10Mg alloy powder is shown in Figure 1a. As shown in Table 3, the median diameter (D_{50}) of AlSi10Mg was evaluated as $\sim 40 \mu\text{m}$. The powder of MoSi_2 consists of agglomerates of fine (1–5 μm) particles (Figure 1b), with $D_{50} < 19 \mu\text{m}$ (Table 3). The SEM image of the MoSi_2 -30 wt.% AlSi10Mg powder mixture clearly demonstrates an apparent particle size difference between constituents. Fine MoSi_2 particles can serve as nucleation centers during cooling and provide homogeneous solidification after laser scanning.

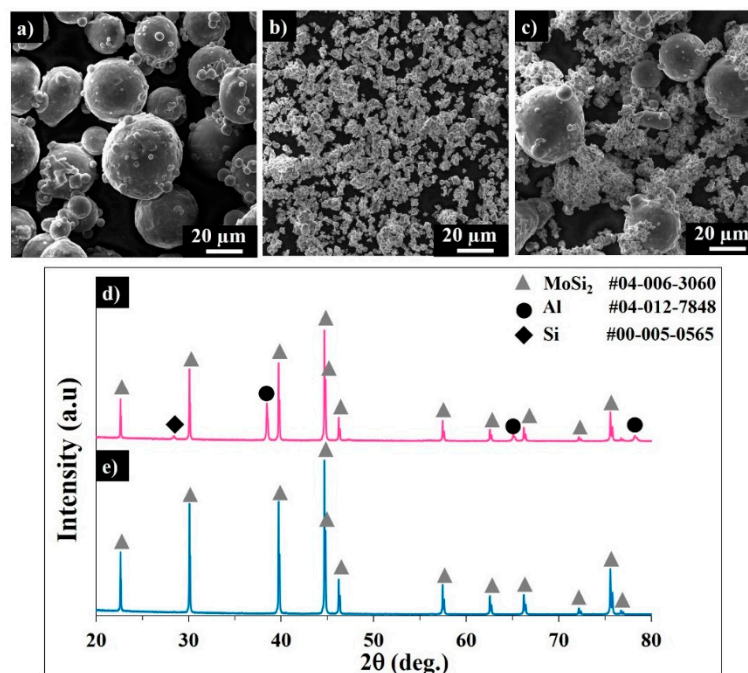


Figure 1. SEM images of the AlSi10Mg alloy (a) MoSi₂ and (b) MoSi₂-30 wt.% AlSi10Mg powder mixture (c). Corresponding XRD patterns of the MoSi₂-30 wt.% AlSi10Mg (d) and MoSi₂ (e) powders.

Table 3. Size distributions of the AlSi10Mg, MoSi₂, and MoSi₂-30 wt.% AlSi10Mg powders.

Composition	Particle Size		
	D10 (μm)	D50 (μm)	D90 (μm)
AlSiMg10	25.14 ± 0.53	38.72 ± 0.67	55.47 ± 0.44
MoSi ₂	5.44 ± 0.26	18.95 ± 0.89	43.45 ± 0.65
MoSi ₂ -30 wt.% AlSi10Mg	7.68 ± 0.07	33.02 ± 1.18	54.19 ± 1.30

Usually, the spherical particles of narrow size distribution exhibit better flowability compared to the angularly shaped powders. The sphericity of the MoSi₂-30 wt.% AlSi10Mg mixture gradually decreased from ~0.9 to 0.79 in a particle size range of 3–55 μm, conditioned by the non-spherical shape of the MoSi₂ agglomerates.

The basic flowability energy values of AlSi10Mg, MoSi₂-30 wt.% AlSi10Mg, and MoSi₂ were not significantly different, being ~206, 252, and 307 mJ, respectively (Table 4). Therefore, the flowability of the mixture can be considered as fair and applicable for SLM processing.

Table 4. Average flow rate for the MoSi₂, MoSi₂-30 wt.% AlSi10Mg, and AlSi10Mg alloy powders.

FT4 Results	Powders		
	MoSi ₂ (<45 μm)	MoSi ₂ -30 wt.% AlSi10Mg	AlSi10Mg (15–63 μm)
BFE, mJ	307.52 ± 13.74	252.27 ± 19.41	206.14 ± 8.92
SI	1.09999 ± 0.00606	0.95012 ± 0.07664	0.96271 ± 0.06536

The bulk density of the powders is another important characteristic when choosing the powder feedstock for SLM. Figure 2 shows the packing density of the MoSi₂-30 wt.% AlSi10Mg powder mixture. The initial bulk density of the powder was 1.76 ± 0.012 g·mL⁻¹; after 2000 taps, the bulk density increased up to 2.45 ± 0.048 g·mL⁻¹ and the packing density was extrapolated to be 2.62 ± 0.064 g·mL⁻¹.

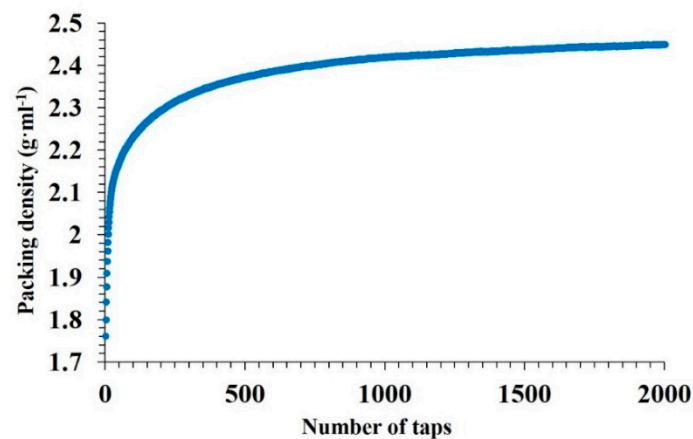


Figure 2. Average packing density of the MoSi₂-30 wt.% AlSi10Mg powder as a function of stress.

Small particles of MoSi₂ can fill voids between the large particles of AlSi10Mg and increase the packing density.

3.2. Bulks

Figure 3 demonstrates the 3D visualization of porosity in samples S1–S3. The porosity level calculated by part and pore voxels is less than 1% when supposing that the relative density of the bulks is $\geq 99\%$. Figure 4 displays X-ray CT analysis of the pore distribution and its aspect ratio. The samples S1 and S3 are printed with the same applied energy density ($100.8 \text{ J}\cdot\text{mm}^{-3}$), but at different scanning speeds and laser powers. The sample S3 possesses the lowest number of pores (Figures 3c and 4), pointing to the effect of the laser power on the decreased porosity; however, further SEM analyses revealed the susceptibility to cracking of the materials printed with a high laser power (300 W). For samples S1 and S2, the maximum frequency was observed for the pores with an aspect ratio of 0.4, while for S3 most of the pores had an aspect ratio of 0.5 (Figure 4c). For all three samples, the majority of the pores measured were of 30 – 35 μm . The relative geometric and Archimedes density results coincided with the CT scanning results (Figure 4d).

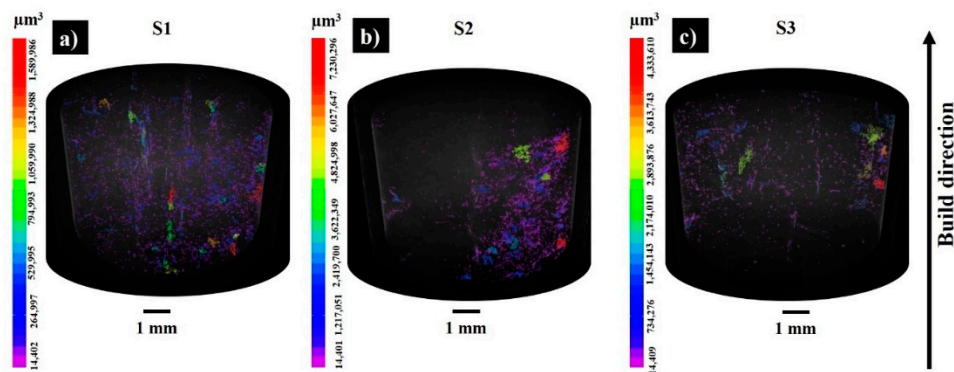


Figure 3. The 3D visualization of the porosity results in as-built samples S1 (a), S2 (b), and S3(c) (pores are labelled by volume (μm^3)).

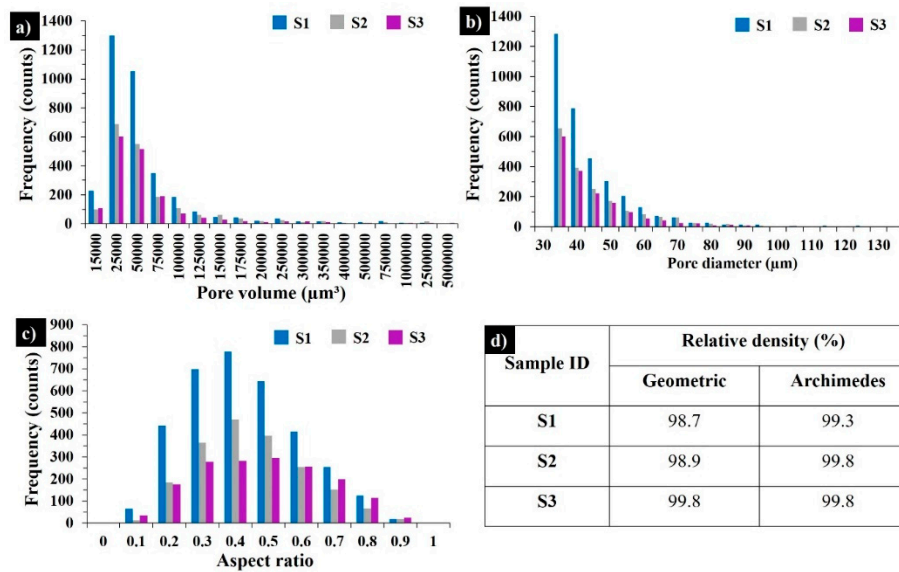


Figure 4. X-ray CT results in as-built samples S1, S2, and S3: pore size distributions (a), pore diameter distributions (b), aspect ratios of the pores (c), and relative geometric and Archimedes density results (d).

The average surface roughness (S_a) and the maximum height (S_z) of the top and side surfaces of the printed samples are listed in Table 5. A two-fold increase in the scanning speed results in a moderate increase in S_a and a dramatic increase in the maximum heights of irregularities for both top and side (vertical) surfaces. S2 produced the highest LED value but a moderate scan speed and possessed the smoothest top surface, which was conditioned by sufficient melting and sintering of the consecutive powder layers. The quality of the side surfaces was slightly inferior compared to the top surface. Particles on the sides were primarily formed by the partial melting at the build surface. For S3, a high applied LED value combined with a high build rate resulted in adhesion of the powder particles from the heat-affected zones onto the side surface of the piece, resulting in high surface roughness. The partially sintered particles detected on the top surface might be due to the blowing of metal particles into the laser-melted zones by the gas flow in the build chamber or from the powder bed due to vibration movement of the wiper during processing. Moreover, aluminum oxide can be formed due to oxidation of AlSi10Mg by the trace oxygen in the inert gas or by the inherent alumina layer on the powder surface. According to the EDS analysis, the adhered particles were examined and determined to be aluminum oxide (Figure 5, Spectrum 1).

Table 5. The roughness of the top and side surfaces of the printed samples.

Sample	Top Surface Roughness, μm		Side Surface Roughness, μm	
	S_a	S_z	S_a	S_z
S1	10.1	94.4	11.2	109.5
S2	9.9	75.5	13.2	130.8
S3	14.7	130.2	17.8	173.5

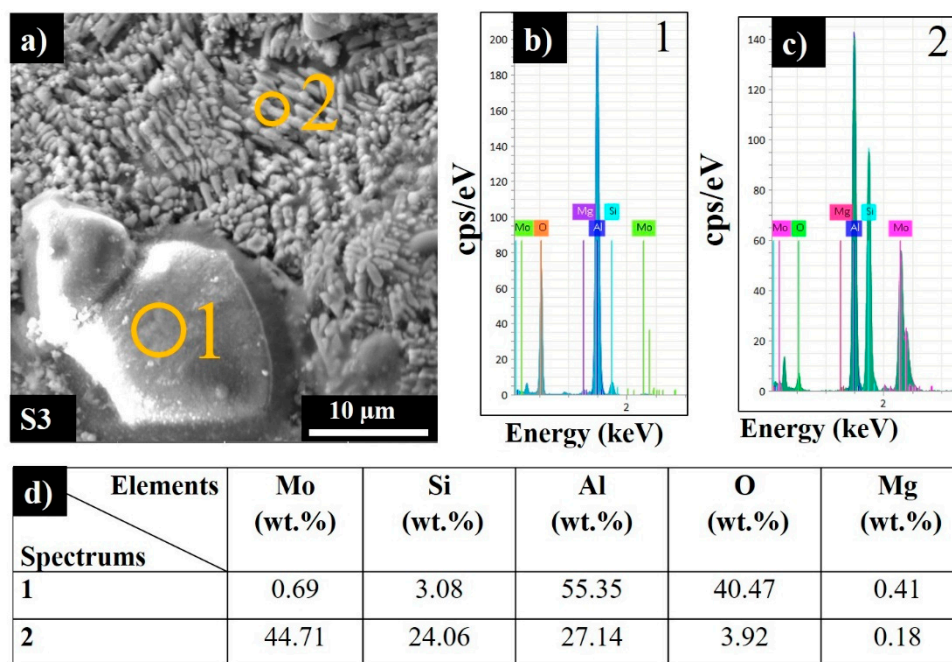


Figure 5. Side surface SEM image (a), EDS spectra (b,c), and corresponding elemental analysis results for sample S3 (d).

Spectrum 2 (Figure 5c) shows that the chosen section was composed of 44.71 wt.% Mo 24.06 wt.% Si and 27.14 wt.% Al, along with 3.92 wt.% oxygen.

3.3. Microstructural Analysis

The SEM images of the polished top surfaces of samples S1, S2, and S3 are depicted in Figure 6. The marked elliptical regions in Figure 6a–c demonstrate the core of the melt pools. The solidification process affects the crystallization in different regions due to various temperature gradients and heat flux directions, depending on the laser power and scanning speed. The melt pool dimensions depend on the applied laser power, LED, and temperature. There was a larger heat flux in the center of the melt pool due to Gaussian intensity of the single mode laser beam; hence, the surface tension varied between the center and outer edges, resulting in multifarious microstructures along the sample. Importantly, controlling the volume of the melt by increasing the scan speed was demonstrated to reduce the overlap and cause insufficient melting (Figure 6c).

The cores consisted of fine submicron- to micron-sized grains (Figure 6d–f), while at the border of each elliptical section, the coarser columnar dendrites were observed (Figure 6d,e). This phenomenon is caused by the cooling rate and temperature difference in the center of the melt pool and at the border, as the melt pool periphery is exposed to a longer laser exposure during overlapping of adjacent scan tracks. From the microstructure of S3 produced at the scan speed of $1000\text{mm}\cdot\text{s}^{-1}$ (Figure 6c), a higher inhomogeneity of the morphological texture was detected as compared to samples S1 and S2. The bright regions in Figure 6 represent sintered MoSi_2 , while the dark grey regions represent the segregated Al-rich phase that developed due to the incomplete reaction between MoSi_2 and Al at high scanning speeds. The light grey phase characterizes the Mo-Si-Al phase (which according to further XRD analysis was found to be the $\text{Mo}_3(\text{Al}_2\text{Si}_4)$ phase). A high scanning speed decreases the interaction time between a laser and a material, thus decreasing the solidification time and inducing a high temperature gradient [20]; therefore, a higher cooling rate at the interface results in a finer microstructure, as seen from Figure 6f.

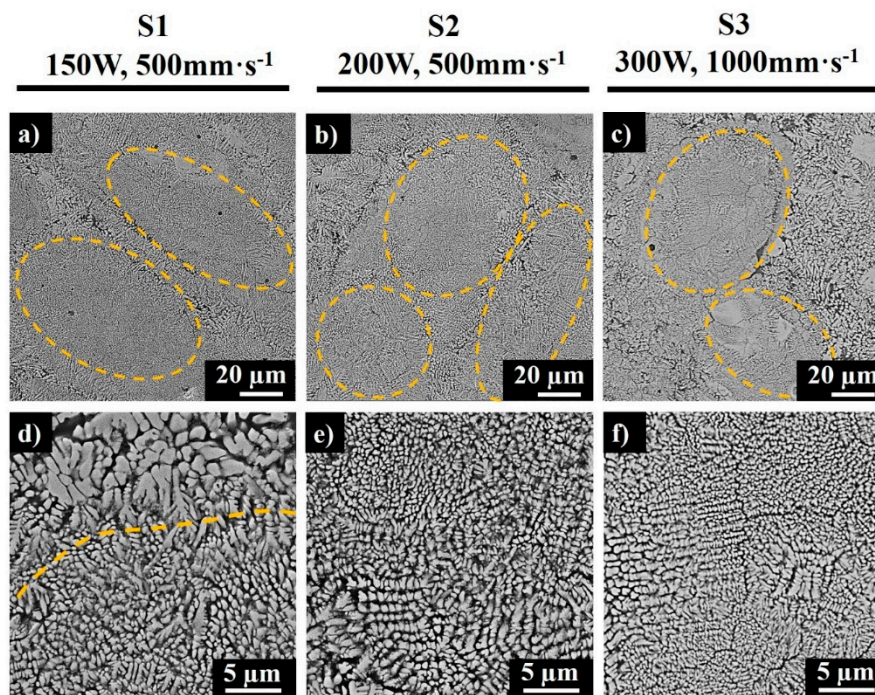


Figure 6. SEM images of polished top surfaces of samples S1 (a,d), S2 (b,e), and S3 (c,f).

Figure 7 demonstrates the backscattered electron (BSE) and secondary electron (SE) images of S2, along with corresponding elemental and mixed EDS maps.

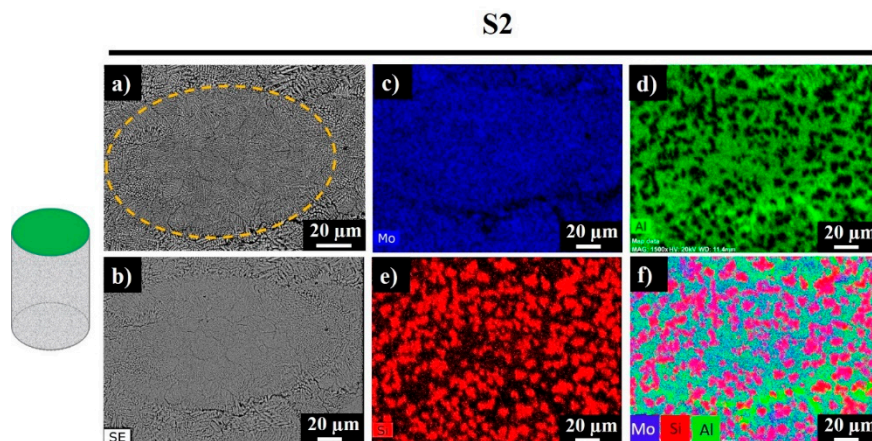


Figure 7. Top surface backscattered electron (BSE) image (a), secondary electron (SE) image (b), and EDS mapping results (c–f) for sample S2.

Signals of Mo were recorded everywhere expect the darkest regions, which correspond to the Al-rich phase (Figure 7d, bright green regions). Silicon was also observed in the studied area, while the bright red sections revealed the existence of replaced free Si, where no Al was detected. Accordingly, the sample was composed of Mo-Si-Al-, Al-, Al-, and Si-rich phases. Figure 8 shows the polished side fracture of sample S2 and the corresponding EDS maps. The yellow dashed regions (Figure 8a,b) represent the melt pools. The core of the melt pool was composed of fine elongated columnar dendrites with secondary arms grown parallel to the build direction, whereas the edges consisted of the coarser columnar dendrites (marked with white arrows) with occasional secondary branching due to overlap with the neighboring melt pools (Figure 8b).

S2

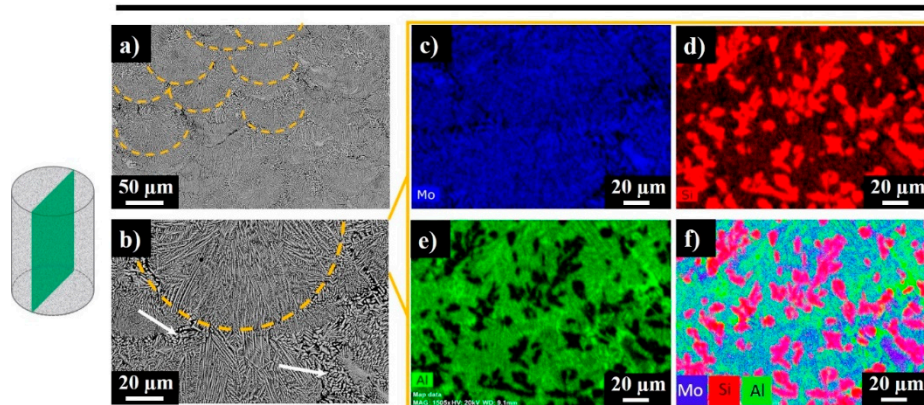


Figure 8. Top surface SEM images (a,b) and EDS mapping results for sample S2 (c–f).

The EDS maps corresponding to the SEM image in Figure 8b reveal a similar composition as for the top surface of the sample. Most of the studied area was composed of the Mo-Si-Al-containing phase. The dark regions in Figure 8b reveal the absence of Mo and the presence of the Al-rich phase. The black regions in the Al green map and the bright red regions in the Si map disclose the partial substitution of Si by Al.

Figure 9 displays the XRD patterns and Table 6 shows the phases and elemental compositions of the samples according to the Rietveld refinement method.

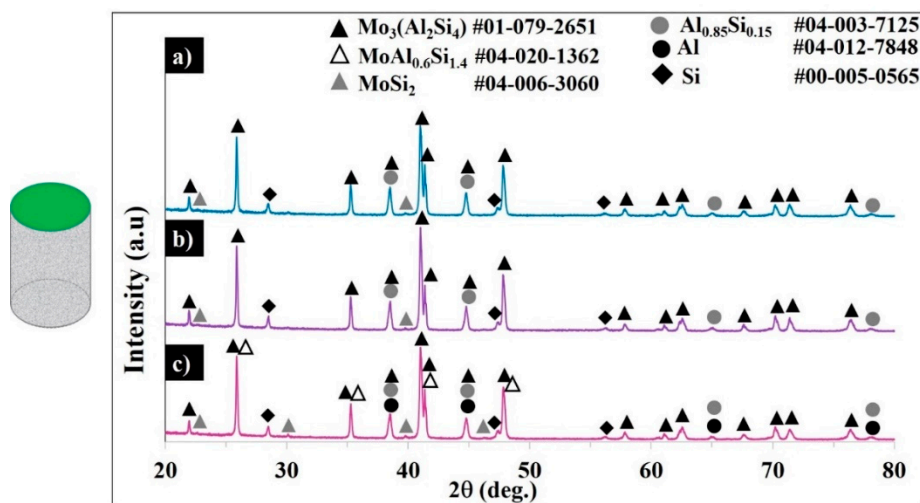


Figure 9. XRD patterns of samples S1 (a), S2 (b), and S3 (c).

Table 6. Compositions of the samples estimated from XRD patterns via the Rietveld refinement method.

Sample ID	Composition (%)						Elemental Composition (%)		
	Mo ₃ (Si ₄ Al ₂)	MoAl _{0.6} Si _{1.4}	MoSi ₂	Al _{0.85} Si _{0.15}	Al	Si	Mo	Si	Al
S1	69.4	0.5	1.2	19.7	0.0	9.1	45.1	30.0	24.9
S2	70.9	0.7	1.1	17.5	0.0	9.7	46.1	30.6	23.3
S3	67.0	3.7	2.4	17.0	1.2	8.7	46.3	29.8	23.9

The diffractograms of sample S3 confirm the presence of tetragonal MoSi₂, face-centered cubic Al, the substituted face-centered Si, the coexistence of the in-situ-formed hexagonal Mo₃(Al₂Si₄)/MoAl_{0.6}Si_{1.4} phases (corresponds to Mo(Si_{1-x}Al_x)₂, x = 0.3–0.33) composition), and the Si-saturated Al-rich Al_{0.85}Si_{0.15} phase.

The patterns for samples S1 and S2 evidenced the complete transformation of MoSi_2 to $\text{C40 Mo}_3(\text{Al}_2\text{Si}_4)$, with weak peaks of unreacted C11b, negligible $\text{MoAl}_{0.6}\text{Si}_{1.4}$, and with $\text{Al}_{0.85}\text{Si}_{0.15}$ being formed. For the applied high scanning speed, apparently the unreacted MoSi_2 and face-centered Al were found in the final product. In samples S1 and S2, no pure Al was detected, but the Si-saturated Al-rich $\text{Al}_{0.85}\text{Si}_{0.15}$ phase was detected. Under the chosen conditions ($100.8\text{--}134.4 \text{ J}\cdot\text{mm}^{-3}$ ED) and with the addition of 30 wt.% AlSi10Mg to the MoSi_2 , the C11b tetragonal lattice of MoSi_2 expanded until achieving a hexagonal $\text{Mo}(\text{Si}_{0.67}\text{Al}_{0.33})_2$ ($x = 0.33$ mol) structure, while no further C40 lattice expansion was detected in forming the Al-rich orthorhombic C54 structure. In contrast, the formation of C54 orthorhombic structures with $\text{Mo}_{10}\text{Si}_7\text{Al}_{13}$, $\text{MoAl}_{1.3}\text{Si}_{0.7}$, and $\text{Al}_4\text{Mo}_3\text{Si}_2$ is claimed in [4,9–11]; the formation of the silicon lean Al_8Mo_3 phase is reported in [14].

To study the mechanism of the $\text{MoSi}_2\text{--AlSi10Mg}$ interaction, the thermogravimetric analysis for $\text{MoSi}_2\text{--}30 \text{ wt.}\% \text{AlSi10Mg}$ was performed. Figure 10a shows the DSC-TG curves of the $\text{MoSi}_2\text{--}30 \text{ wt.}\% \text{AlSi10Mg}$ mixture heated up to $1450 \text{ }^\circ\text{C}$. The DSC curves exhibit the endothermic peak of the reaction of the aluminum melting and the Al-Si eutectic phase formation, where the heat absorption recorded was $0.9575 \text{ W}\cdot\text{g}^{-1}$. The weak exothermic reaction was observed starting from $944 \text{ }^\circ\text{C}$ and the maximum heat flow was $0.2393 \text{ W}\cdot\text{g}^{-1}$ at $1019 \text{ }^\circ\text{C}$.

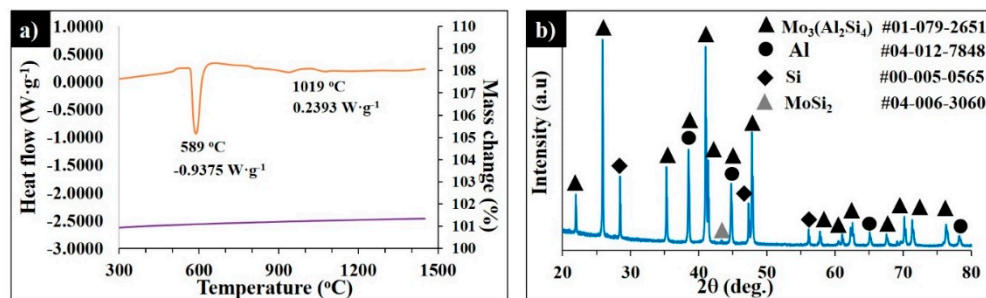


Figure 10. DSC-TG curves of $\text{MoSi}_2\text{--}30 \text{ wt.}\% \text{AlSi10Mg}$ heated up to $1450 \text{ }^\circ\text{C}$ at $20^\circ \cdot \text{min}^{-1}$ in Ar (a) and the corresponding XRD pattern of the quenched sample (b).

No further chemical reactions were detected. According to the XRD patterns in Figure 10b, the sample contained 62.4% $\text{Mo}_3(\text{Al}_2\text{Si}_4)$, 0.7% MoSi_2 , 12.4% Si, 3.3% $\text{MoAl}_{0.6}\text{Si}_{1.4}$, and 21.2% Al; however, the $\text{Al}_{0.85}\text{Si}_{0.15}$ phase was not detected.

The measured hardness of all SLM-processed materials was $\text{HV1} \sim 545 \pm 48$, which was around four times higher than for the printed AlSi10Mg alloy [21]. The high hardness is attributed to the significant effect of the MoSi_2 addition and the development of new phases during solidification.

4. Conclusions

Nowadays, there is huge interest in the development of new alloys for AM processes. The in situ SLM of mixed powders allows the production of hard materials with tailored properties, taking into consideration specific needs.

Fully dense $\text{Mo}(\text{Si}_{1-x}\text{Al}_x)_2$ -based composites with hardness exceeding 500 HV1 were successfully SLM-processed at laser volumetric energy density values of 100.8 and $134.4 \text{ J}\cdot\text{mm}^{-3}$ and with scanning speeds of either 500 or 1000 mm s^{-1} from a $\text{MoSi}_2\text{--}30 \text{ wt.}\% \text{AlSi10Mg}$ powder mixture. The bulks demonstrated relatively low roughness for both the top (horizontal) and side (vertical) surfaces, indicating the good quality of the produced parts.

Under the chosen conditions, with the addition of 30 wt.% AlSi10Mg to the MoSi_2 , the C11b tetragonal lattice of MoSi_2 was expanded until achieving a hexagonal $\text{Mo}(\text{Si}_{0.67}\text{Al}_{0.33})_2$ ($x = 0.33$ mol) structure, while no further C40 lattice expansion was detected in forming the Al-rich orthorhombic C54 structure.

Author Contributions: Conceptualization, I.H. and S.A.; methodology, T.M., S.A., and E.T.; software, T.M.; validation, I.H., S.A., and E.T.; formal analysis, T.M.; investigation, T.M.; resources, I.H. and E.T.; data curation,

I.H.; writing—original draft preparation, T.M.; writing—review and editing, I.H., and S.A.; visualization, T.M.; supervision, I.H. and S.A.; project administration, E.T. and I.H.; funding acquisition, I.H., and S.A. All authors have read and agreed to the published version of the manuscript.

Funding: This research was funded by the Estonian Research Council, grants PSG220 (S.A.) and PRG643. (I.H.).

Acknowledgments: This work was supported by the Estonian Research Council PSG220 (S.A.), PRG643 (I.H.). T.M. acknowledges the Archimedes foundation under the DORA + scholarship program for funding the travel visit to the University of Waterloo (Canada). The authors would like to thank also Rainer Traksmäa, Henry Ma and Ehsan Marzbanrad for their help with XRD, CT scanning, and DSC analyses.

Conflicts of Interest: The authors have no conflict of interest to declare.

References

1. Yao, Z.; Stiglich, J.; Sudarshan, T.S. Molybdenum silicide based materials and their properties. *J. Mater. Eng. Perform.* **1999**, *8*, 291–304. [[CrossRef](#)]
2. Vasudevan, A.K.; Petrovic, J.J. A comparative overview of molybdenum disilicide composites. *Mater. Sci. Eng. A* **1992**, *155*, 1–17. [[CrossRef](#)]
3. Maruyama, T.; Yanagihara, K. High temperature oxidation and peeling of Mo(Si,Al)₂. *Mater. Sci. Eng. A* **1997**, *239*, 828–841. [[CrossRef](#)]
4. Stergiou, A.; Tsakirooulos, P. Study of the effects of Al, Ta, W additions on the microstructure and properties of MoSi₂ base alloys. *MRS Online Proc. Libr. Arch.* **1994**, *364*, 991. [[CrossRef](#)]
5. Harada, Y.; Murata, Y.; Morinaga, M. Solid solution softening and hardening in alloyed MoSi₂. *Intermetallics* **1998**, *6*, 529–535. [[CrossRef](#)]
6. Sharif, A.A.; Misra, A.; Petrovic, J.J.; Mitchell, T.E. Alloying of MoSi₂ for improved mechanical properties. *Intermetallics* **2001**, *9*, 869–873. [[CrossRef](#)]
7. Ramberg, C.E.; Worrell, W.L. Fabrication and High-Temperature Phase Stability of Mo (Al, Si) ₂—MoSi₂ Intermetallics. *J. Am. Ceram. Soc.* **2000**, *83*, 946–948. [[CrossRef](#)]
8. Hobosyan, M.A.; Khachatryan, H.L.; Davidova, A.; Kharatyan, S.L. Chemically activated combustion synthesis of MoSi₂/Al cermet foams. *Chem. Eng. J.* **2011**, *170*, 286–291. [[CrossRef](#)]
9. Hou, H.D.; Ning, X.J.; Wang, Q.S.; Bin, G.A.O.; Liu, Y.B.; Ying, L.I.U. Preparation of Mo(Si,Al)₂ feedstock used for air plasma spraying. *Trans. Nonferrous Met. Soc.* **2016**, *26*, 2939–2946. [[CrossRef](#)]
10. Ghayoumabadi, M.E.; Saidi, A.; Abbasi, M.H. Lattice variations and phase evolutions during combustion reactions in Mo–Si–Al system. *J. Alloys Compd.* **2009**, *472*, 84–90. [[CrossRef](#)]
11. Tabaru, T.; Shobu, K.; Sakamoto, M.; Hanada, S. Effects of substitution of Al for Si on the lattice variations and thermal expansion of Mo(Si,Al)₂. *Intermetallics* **2004**, *12*, 33–41. [[CrossRef](#)]
12. Wang, X.H.; Wu, G.Z.; Lu, Q.; Sun, Z. Synthesis and mechanical properties of Nb and Al substituted MoSi₂. *Mater. Res. Innov.* **2015**, *19* (Suppl. 4), S175–S180. [[CrossRef](#)]
13. Nanko, M.; Kitahara, A.; Ogura, T.; Kamata, H.; Maruyama, T. Formation of Mo(Si,Al)₂ layer on Mo dipped in Al melt saturated with Si and the effects of transition metals added in the melt. *Intermetallics* **2001**, *9*, 637–646. [[CrossRef](#)]
14. Liu, Y.; Shao, G.; Tsakirooulos, P. Thermodynamic reassessment of the Mo–Si and Al–Mo–Si systems. *Intermetallics* **2000**, *8*, 953–962. [[CrossRef](#)]
15. Minasyan, T.; Aghayan, M.; Liu, L.; Aydinyan, S.; Kollo, L.; Hussainova, I.; Rodríguez, M.A. Combustion synthesis of MoSi₂ based composite and selective laser sintering thereof. *J. Eur. Ceram. Soc.* **2018**, *38*, 3814–3821. [[CrossRef](#)]
16. Minasyan, T.; Liu, L.; Holovenko, Y.; Aydinyan, S.; Hussainova, I. Additively manufactured mesostructured MoSi₂-Si₃N₄ ceramic lattice. *Ceram. Int.* **2019**, *45*, 9926–9933. [[CrossRef](#)]
17. Read, N.; Wang, W.; Essa, K.; Attallah, M.M. Selective laser melting of AlSi10Mg alloy: Process optimisation and mechanical properties development. *Mater. Des.* **2015**, *65*, 417–424. [[CrossRef](#)]
18. ISO 13322-2. Particle Size Analysis—Image Analysis Methods—Part 2: Dynamic Image Analysis Methods. International Organization for Standardization: Geneva, Switzerland, 2006.
19. Aboulkhair, N.T.; Everitt, N.M.; Ashcroft, I.; Tuck, C. Reducing porosity in AlSi10Mg parts processed by selective laser melting. *Addit. Manuf.* **2014**, *1*, 77–86. [[CrossRef](#)]

20. Zhang, J.; Song, B.; Wei, Q.; Bourell, D.; Shi, Y. A review of selective laser melting of aluminum alloys: Processing, microstructure, property and developing trends. *J. Mater. Sci. Technol.* **2019**, *35*, 270–284. [[CrossRef](#)]
21. Liu, B.; Li, B.Q.; Li, Z. Selective laser remelting of an additive layer manufacturing process on AlSi10Mg. *Results Phys.* **2019**, *12*, 982–988. [[CrossRef](#)]



© 2020 by the authors. Licensee MDPI, Basel, Switzerland. This article is an open access article distributed under the terms and conditions of the Creative Commons Attribution (CC BY) license (<http://creativecommons.org/licenses/by/4.0/>).